TEXTILES

Spectrally engineered textile for radiative cooling against urban heat islands

Ronghui Wu[1]†, Chenxi Sui[1]†, Ting-Hsuan Chen[1,2], Zirui Zhou[1], Qizhang Li[1], Gangbin Yan[1], Yu Han[1], Jiawei Liang[2], Pei-Jan Hung[1], Edward Luo[1], Dmitri V. Talapin[1,3,4], Po-Chun Hsu[1]*

Radiative cooling textiles hold promise for achieving personal thermal comfort under increasing global temperature. However, urban areas have heat island effects that largely diminish the effectiveness of cooling textiles as wearable fabrics because they absorb emitted radiation from the ground and nearby buildings. We developed a mid-infrared spectrally selective hierarchical fabric (SSHF) with emissivity greatly dominant in the atmospheric transmission window through molecular design, minimizing the net heat gain from the surroundings. The SSHF features a high solar spectrum reflectivity of 0.97 owing to strong Mie scattering from the nano-micro hybrid fibrous structure. The SSHF is 2.3°C cooler than a solar-reflecting broadband emitter when placed vertically in simulated outdoor urban scenarios during the day and also has excellent wearable properties.

The urban heat island effect has emerged as a large concern with respect to its effect on the thermal homeostasis of the human body, exacerbating the effects of global warming. This phenomenon leads to a range of heat-related illnesses, including cardiovascular mortality, respiratory illnesses, neurological disorders, and injuries (*1*–*4*). One main cause of the urban heat island effect is that urban infrastructures, such as buildings and the ground, absorb a greater amount of solar radiation and reemit more to the ambient than natural landscapes like grasses, trees, and water bodies (*5*–*7*). The effect not only amplifies heat waves that result in higher morbidity and mortality risk but also has substantial implications for energy consumption, air quality, and urban ecosystems (*8*–*16*). Presently, more than half of the world's population resides in cities (*17*). With increasing urbanization in all countries projected to grow from 57% in 2022 to 68% by 2050 (*18*), a greater proportion of people worldwide will be exposed to the urban heat island effect, with increased risks from heat extremes in urban areas in the near future (*19*). Therefore, taking proactive measures to stay healthy against the urban heat island effect is crucial for contemporary society.

One promising approach to maintaining thermal comfort is through radiative cooling textiles that emit thermal radiation into outer space and reject solar radiation (*20*–*39*). Outstanding passive daytime radiative cooling performance has been demonstrated under a clear sky (*40*–*43*), but heat gain from the heated ground and urban structures is generally not taken into account. Specifically, the radiative cooling textiles were often designed as broadband emitters in the entire mid-infrared (MIR) region and assumed to have an unobstructed view of the sky. Therefore, their cooling performance, including cooling power and temperature reduction, is normally described for horizontal geometry. This assumption neglects that around 97% of textiles from a fully clothed standing person are typically used vertically (*44*, *45*). Only a small amount of the cloth area (<3%) is horizontally oriented, usually from hats, cloth on the shoulders, and shoe coverings (Fig. 1, A and B). Therefore, in an open scenario, 50% of the field of view of the apparel is toward the territory objects, that is, the ground (Fig. 1A), and this proportion increases even more in an urban scenario because of the buildings and other infrastructure (Fig. 1B). These human-made structures, when exposed to intense solar radiation, can reach high temperatures that exceed 70°C and emit substantial amounts of heat (*46*). For example, thermographs representing different landscapes in Apache Junction, Arizona, show that urban terrestrial objects are much hotter than human skin, thereby working as heat sources for the human body (Fig. 1C and fig. S1). According to Kirchhoff's law, emissivity equals absorptivity at thermodynamic equilibrium. In other words, the cooling performance of a broadband-emissive textile will often be greatly compromised by the incoming thermal radiation from the surroundings. To achieve high cooling performance for clothes for more realistic scenarios, spectrum-selective textiles should be designed such that emission is only dominant in the atmospheric transmission window (ATW) of the wavelength range 8 to 13 μm, and all the non-ATW parasitic heat from the surrounding ground or buildings is suppressed. This concept was brought up by Mandal *et al.* for building facades (*47*), but demonstrating the same photonic design for human body cooling is nontrivial. For human body cooling, stringent material requirements exist for wearability, breathability, and flexibility, and rigorous optical engineering is needed because of the intricacies of human body–textile microclimates.

We designed a MIR spectrally selective hierarchical textile (SSHF) that has a high ATW spectral selectivity ratio of 2.23 and an average ATW emissivity of 0.85, thereby providing a pronounced cooling effect in urban areas. The high emissivity in the ATW region allows the SSHF to emit heat to outer space, and high reflectivity (low absorptivity) in the non-ATW region minimizes the heat absorption from the surrounding hot ground or buildings. We designed the SSHF based on multimodal heat transfer mechanisms and light-matter interaction; it consists of a polymethylpentene (PMP) nano-micro hybrid fibrous layer, silver nanowires (AgNWs), and wool fabric. The surface PMP fibers have a wide range of size distributions owing to the sequential volatilization of solvents during electrospinning, which enables a wideband scattering efficiency that covers the entire solar spectrum. PMP only has C–C (954 to 1004 cm^{-1}), $-CH_2$ (1176 to 1241 cm^{-1}), –CH (862 to 881 cm^{-1}), and $-CH_3$ (931 cm^{-1}) bonds, so it shows great potential as a selective emitter with high absorption only in the ATW range. The middle AgNW layer provides a high reflectivity in the whole MIR region, preventing infrared (IR) transmission from urban infrastructures to the human body. The bottom wool fabric is a broadband emitter, which absorbs thermal radiation from the human skin through the textile-skin air gap (*48*) and further conducts the heat to the top PMP fabric via the AgNW layer.

Importance of spectrally selective textiles

We theoretically calculated ground and building temperatures by taking the most common infrastructure materials as an example, such as concrete and asphalt [fig. S2; see text in (*49*)]. When the solar intensity reaches 300 W m^{-2} with an ambient temperature of 303.15 K (30°C), which is common on a typical sunny day, ground and building temperatures can readily surpass the average temperature of human skin. Therefore, the effect of such infrastructure heat sources on the cooling performance of traditional broadband-emissive textiles, such as cotton, silk, and polyester fabrics, is substantial. The reason for this is that the high broadband emissivity of these textiles will result in considerable heat gain from the environment based on Kirchhoff's radiation law. Although a broadband emitter (blue dashed line) can result in heat loss through the ATW (8 to 13 μm) to outer space (Fig. 1D) (*50*), substantial heat gain still occurs from the surrounding ground and buildings within the wavelength ranges of 2.5 to 8 μm and 13 to

[1]Pritzker School of Molecular Engineering, University of Chicago, Chicago, IL 60637, USA. [2]Thomas Lord Department of Mechanical Engineering and Materials Science, Duke University, Durham, NC 27708, USA. [3]Department of Chemistry and James Franck Institute, University of Chicago, Chicago, IL 60637, USA. [4]Center for Nanoscale Materials, Argonne National Laboratory, Argonne, IL 60439, USA.
*Corresponding author. Email: pochunhsu@uchicago.edu
†These authors contributed equally to this work.

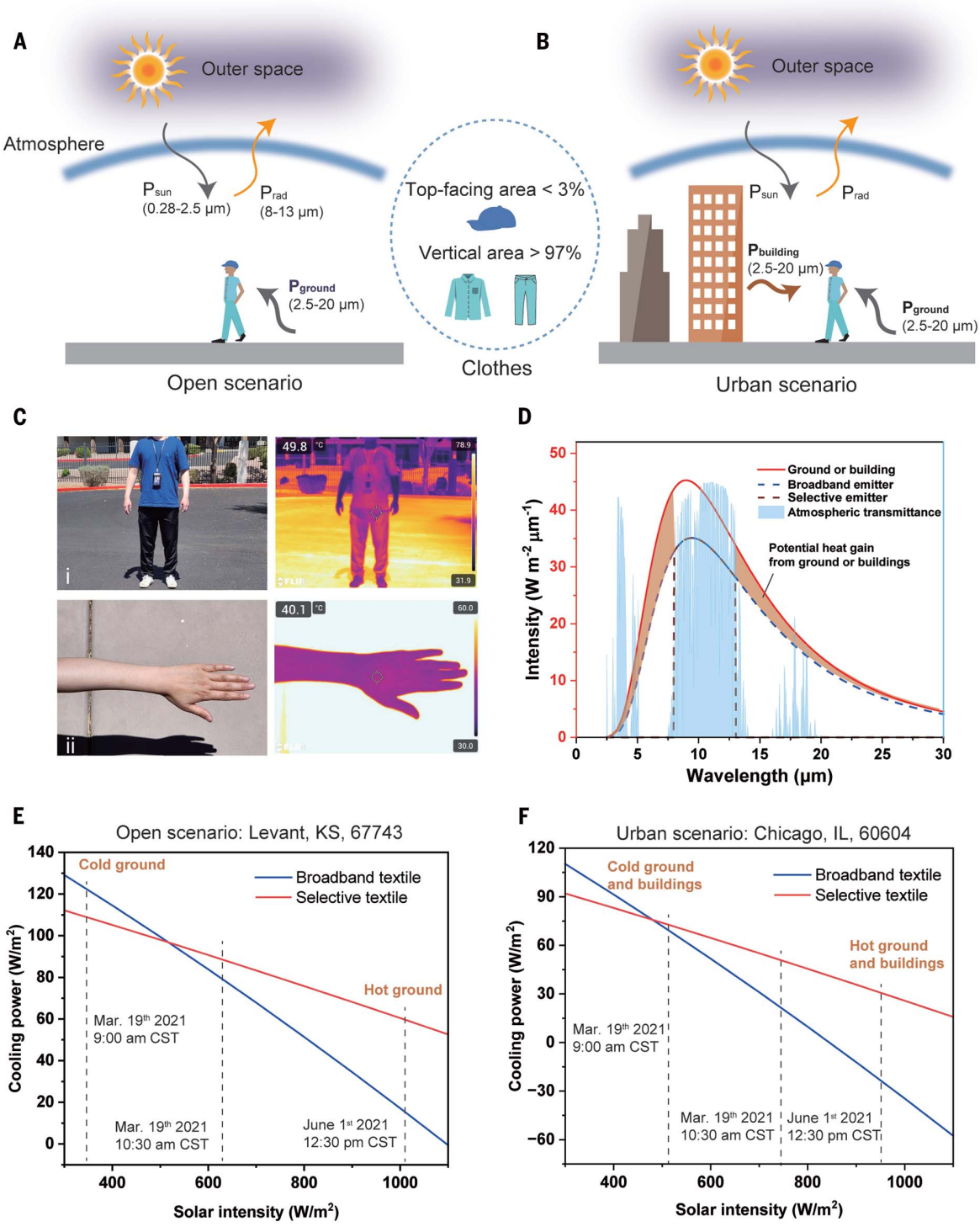

Fig. 1. Concept and advantages of a spectrally selective textile for vertically oriented fabrics for radiative cooling. (**A** and **B**) Schematic of wearable fabrics in an open scenario (A) and an urban scenario (B). P, power; rad, radiation. (**C**) Optical (left) and IR (right) images of characteristic urban scenarios in Apache Junction, Arizona, showing that terrestrial objects work as a heat source for the human body. The images were taken at (i) 14:13 p.m. MST on 29 May 2023 at 33.41° N, 111.60° W (elevation of 480 m) and (ii) 12:35 p.m. MST on 29 May 2023 at 33.44° N, 111.48° W (elevation of 635 m). (**D**) The radiated power from a perfect broadband or spectrum-selective textile emitter at a human skin temperature T_{skin} of 34°C and hemispherical irradiances from the terrestrial features at an effective radiative temperature T_{terr} of 50°C. (**E**) Calculated cooling power for broadband and selective vertically oriented textiles versus solar intensity in an open scenario, such as Levant, Kansas. Solar intensities from 19 March and 1 June 2021 were selected for better clarity. (**F**) Calculated cooling power for vertically oriented broadband and selective textiles in an urban scenario, such as downtown Chicago, Illinois. (Note that in the context of cooling power, a positive value indicates that the sample is being cooled.)

20 μm. We simplified the ATW wavelength range to 8 to 13 μm because the spectral emissive power in the 3- to 4-μm range for human body radiation is much lower. Therefore, to minimize heat gain from the ambient while maintaining heat emission to outer space through the ATW (brown dashed line in Fig. 1D), the radiative cooler should selectively emit in the ATW and reflect in non-ATW wavelengths (fig. S4). We compared the cooling power performance of a vertically placed broadband-emissive textile and the MIR spectrally selective–emissive textile under different solar illumination conditions [see text in (*49*)]. The broadband textile has an emissivity of unity in the whole MIR wavelength range (2.5 to 20 μm), whereas we assume the selective textile to be an ideal selective emitter that has an emissivity of 1 in the ATW wavelength range and zero in the non-ATW wavelength range (fig. S4). When the vertical textiles are exposed to an open scenario surrounded by asphalt ground, the broadband textile initially shows a higher cooling power than the selective textile under low-solar-intensity illumination. However, when the solar intensity exceeds the cross-point 520 W m^{-2} (where the cooling demand is reasonably higher), the selective-emissive textile shows a higher cooling power due to its capability to selectively block the radiation emitted by the hot ground (~49°C) (Fig. 1E and fig. S2). For example, for the weather data of Levant, Kansas (from the National Solar Radiation Database) at 9:00 a.m. CST on 19 March 2021, the broadband-emissive textile showed a higher cooling potential than the selective one. However, at 10:30 a.m. CST, the cooling power of the selective textile exceeded that of the broadband-emissive textile. At 12:30 p.m. CST on 1 June 2021, the cooling power gap between the broadband- and selective-emissive cloths further increased to 44.1 W m^{-2}. When vertical textiles are exposed to an urban scenario, where buildings are densely distributed, the heat-gain phenomenon is even more pronounced (Fig. 1F). For example, assuming that the distance between the vertical textile and a building wall made of dark brown brick is 1.7 times the building height and that the building width is 2.8 times the height, the cross-point cooling power point shifts to 480 W m^{-2} of the solar radiation intensity. Therefore, the cooling power difference between the broadband- and selective-emissive cloths reached 54.1 W m^{-2} at 12:30 p.m. CST on 1 June 2021. Our calculations show the importance and efficacy of selective textiles for wearable personal radiative cooling in urban areas.

MIR spectrum selectivity and ultraviolet-visible reflectivity of PMP fabrics

The preparation of a MIR spectrally selective textile demands a spinnable and robust polymer material with proper chemical bonding that results from meticulous molecular level design (Fig. 2). Typically, such a polymer should have chemical bond vibrations only within the ATW range (8 to 13 μm) (*51*–*54*). However, most natural and synthetic textiles exhibit a large amount of chemical bond vibrations outside of this range, such as –OH (3100 to 3600 cm^{-1}) in cotton, –CONH– (1520 to 1720 cm^{-1}) in silk and wool, C=O (1725 to 1780 cm^{-1}) in polyester (PET) and polyimide (PI), –CN (2240 cm^{-1}) in polyacrylonitrile, and $-CF_2$ (507 to 640 cm^{-1}) in polytetrafluoroethylene (PTFE) (Fig. 2B and table S1). Therefore, these textiles normally show broadband emissivity. Among all the polymer candidates for textile materials, PMP with only C–C (stretching in 942 to 1066 cm^{-1}), $-CH_2$ (twisting and wagging in 1168 to 1241 cm^{-1}), –CH (bending dominant in 848 to 871 cm^{-1}), and $-CH_3$ (rocking in 931 cm^{-1} and twisting in 1103 to 1150 cm^{-1}) bonds shows great potential for achieving the desired selective-emissivity spectrum (*55*, *56*) (Fig. 2, A and B, and tables S2 and S3). To further investigate the optical properties of PMP, we derived complex refractive indices [both visible (vis) and MIR regions] from the optical data of spectroscopic ellipsometry and transmittance spectra. The detailed extraction process and results can be found in figs. S5 and S6 [see text in (*49*)]. We show the fitted real (n) and imaginary (k) parts of the refractive indices of PMP in Fig. 2C. Based on the intrinsic complex refractive index, we used the effective medium theory to calculate the emissivity of PMP, which indeed shows a substantial overlap with the ATW (Fig. 2D). We verified this further experimentally with PMP films of different thicknesses (fig. S7).

To quantitatively compare the emissivity of PMP and other commonly used polymer and textile materials, we defined selective ratio γ as the ratio of the average ATW emissivity (8 to 13 μm) to the non-ATW emissivity (2.5 to 8 μm and 13 to 20 μm):

$$\gamma = \frac{\left(\int_{8\mu m}^{13\mu m} \varepsilon(\lambda) d\lambda\right) / \left(\int_{8\mu m}^{13\mu m} d\lambda\right)}{\left(\int_{2.5\mu m}^{8\mu m} \varepsilon(\lambda) d\lambda + \int_{13\mu m}^{20\mu m} \varepsilon(\lambda) d\lambda\right) / \left(\int_{2.5\mu m}^{8\mu m} d\lambda + \int_{13\mu m}^{20\mu m} d\lambda\right)} \quad (1)$$

where ε(λ) is the emissivity at wavelength λ. The MIR spectrum and thickness of these polymer films or textiles are listed in fig. S8. Among the 10 polymer materials, PMP shows the highest selective ratio of 2.34 (Fig. 2E), followed by polyethylene oxide (PEO) and polypropylene (PP). Natural textile materials, such as cotton, silk, wool, and synthetic textile PET, all exhibit a ratio close to 1, indicating their broadband-emissive characteristics. Assuming that these materials are vertically used and exposed to an urban scenario with a ground and building temperature of 328 K (55°C), PMP yields the highest cooling power of 46.3 W m^{-2} (Fig. 2E) [see text in (*49*)]. This performance is 77.3% of the theoretical limit of an ideal selective fabric (59.9 W m^{-2}).

We used a scalable electrospinning technique to fabricate the PMP polymer into textiles. We first dissolved PMP polymer and tetrabutylammonium bromide (TBAB) in a mixed solution of dimethylformamide (DMF), cyclohexane, and acetone (*49*) and then extruded and stretched the mixture into uniform ribbon-shaped nano-micro hybrid fibers under a strong electrical field. TBAB decreases the surface tension and improves the solution's conductivity, thereby diminishing the Rayleigh instability during the unstable jet movement and facilitating uniform and bead-free PMP fiber formation. We used x-ray nano–computed tomography (nano-CT) and scanning electron microscopy (SEM) (Fig. 2, F and G) to show that PMP fabric has a porous structure, with irregular twists on a single fiber, which is caused by the volatilization speed of different solvents (fig. S9A). Fiber dimension plays a very important role in ensuring an ideal optical spectrum because a selective radiative cooling textile requires a high emissivity (low reflectivity) in the ATW range and a high reflectivity in the ultraviolet–vis–near-infrared (UV-vis-NIR) range. Therefore, we engineered fiber morphology by manipulating the spinning conditions, including solution conductivity, surface tension, flow rate, electric field strength, and polymer concentration [see text in (*49*)]. For instance, fiber dimension decreases substantially when the concentration drops from 2.5 to 1 wt % (Fig. 2H and fig. S10). Specifically, when the concentration is 1.5 wt %, the fiber has an average width of 720 nm and a thickness of 113 nm, based on the fiber-size statistical distribution (fig. S10). This smaller cross-sectional area results in a considerably lower scattering in the ATW (8 to 13 μm) than that of the fibers fabricated using a 2 wt % concentration, based on COMSOL Multiphysics finite element modeling (Fig. 2H and fig. S11) (*49*). In addition, a PMP fiber with this dimension has a high scattering efficiency at the wavelength of 500 nm, near the peak wavelength of the solar spectrum (Fig. 2I and fig. S12). The randomly stacked and twisted multilayer nano-micro hierarchical fibers with broadly distributed fiber sizes result in strong sunlight scattering, and the whole fabric shows a white color (Fig. 2J). The UV-vis-NIR spectrum (Fig. 2J) shows that the weight-averaged solar reflectivity reaches 97% (with respect to the AM1.5 spectrum) when the PMP fabric thickness is 292 μm. At this thickness, the average emissivity of PMP fabric in the ATW range is 85.3%, accompanied by a notably high selective ratio of 2.23 (Fig. 2K).

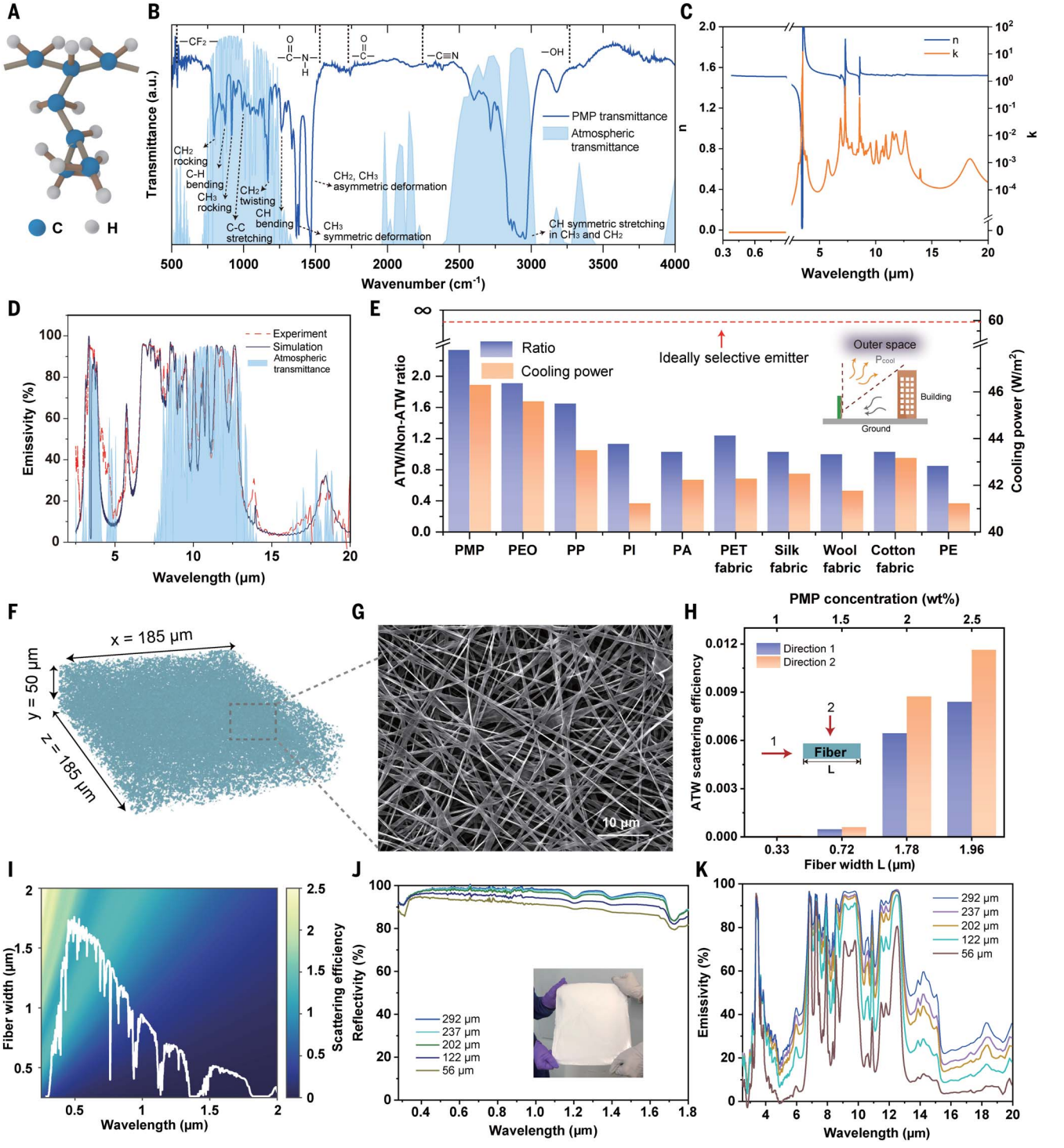

Fig. 2. MIR spectral selectivity and solar reflectivity of PMP fabric. (**A**) Molecular structure of PMP. (**B**) Transmittance spectrum of PMP in the IR wavelength range. Most of the chemical bond vibrational modes resonate within the ATW range, which indicates promising potential for spectrum selectivity. Some typical polymer chemical bonds are outside of the ATW range and thus need to be excluded for a selective emitter, such as amide (–CONH–), ester (–COO–), and nitrile (–CN), as labeled. a.u., arbitrary units. (**C**) Real (*n*) and imaginary (*k*) parts of the refractive indices of PMP extracted by fitting the transmittance spectra and spectroscopic ellipsometry data. (**D**) Both experimental and theoretical results (calculated based on effective medium theory) show that the emissivity of PMP predominantly overlaps with the ATW. (**E**) The emissivity selective ratio and theoretical cooling power for PMP, common polymer films, and textile materials. Calculation of the cooling power takes into consideration the heat gain from the ground and building (T = 328.15 K) and the heat loss to outer space (T = 3 K). The material temperature is set as skin temperature (307.15 K), and the ambient temperature is set as 303.15 K. PA, polyamide; PE, polyethylene. (**F** and **G**) Nano-CT (F) and SEM (G) images showing the irregular morphology of the PMP fibers that were prepared by electrospinning. (**H**) Theoretical scattering efficiency of a PMP fiber in the wavelength range of 8 to 13 μm at two different incident directions, each obtained by averaging different polarizations. (**I**) Theoretical scattering efficiency of PMP fibers in the UV-vis-NIR wavelength, obtained by averaging different incidental directions and polarizations. (**J**) UV-vis-NIR reflectivity of PMP fabric with different thicknesses. The inset is a photo showing the white appearance of the electrospun PMP fabric. (**K**) MIR emissivity of PMP fabric with different thicknesses.

Optical design rationale and SSHF wearable properties

In addition to selective emissivity, other characteristics of heat exchange with the human body and textile wearability are also crucial. For example, although PMP is selectively emissive in the 8- to 13-μm wavelength range, it is transparent rather than reflective in the non-ATW regime. In this case, the human skin (a nearly perfect blackbody) beneath the textile directly absorbs the thermal radiation and compromises the entire concept of a selective emitter. Hence, we engineered the SSHF by integrating PMP fabric, AgNWs, and a wool fabric layer into a multilevel fabric (Fig. 3A). The optical design rationale is to use PMP to achieve outward-facing emissivity in the ATW, AgNWs to suppress the outward-facing non-ATW emissivity (which equals absorptivity), and wool fabric to ensure the inward-facing broadband emissivity (Fig. 3B). The inward-facing fabric is not limited to wool fabric. It can be replaced with fabrics that feature broadband emissivity, such as cotton, nylon, silk, and so on (fig. S13). All these SSHFs have a high and selective outward-facing emissivity and a broadband inward-facing emissivity and therefore can work similarly to the SSHF with wool fabric. With its selective and asymmetrical designs (*57*), SSHF efficiently emits heat to outer space while largely suppressing radiative heat gain and enhancing human body heat loss, as shown in the radiative heat transfer

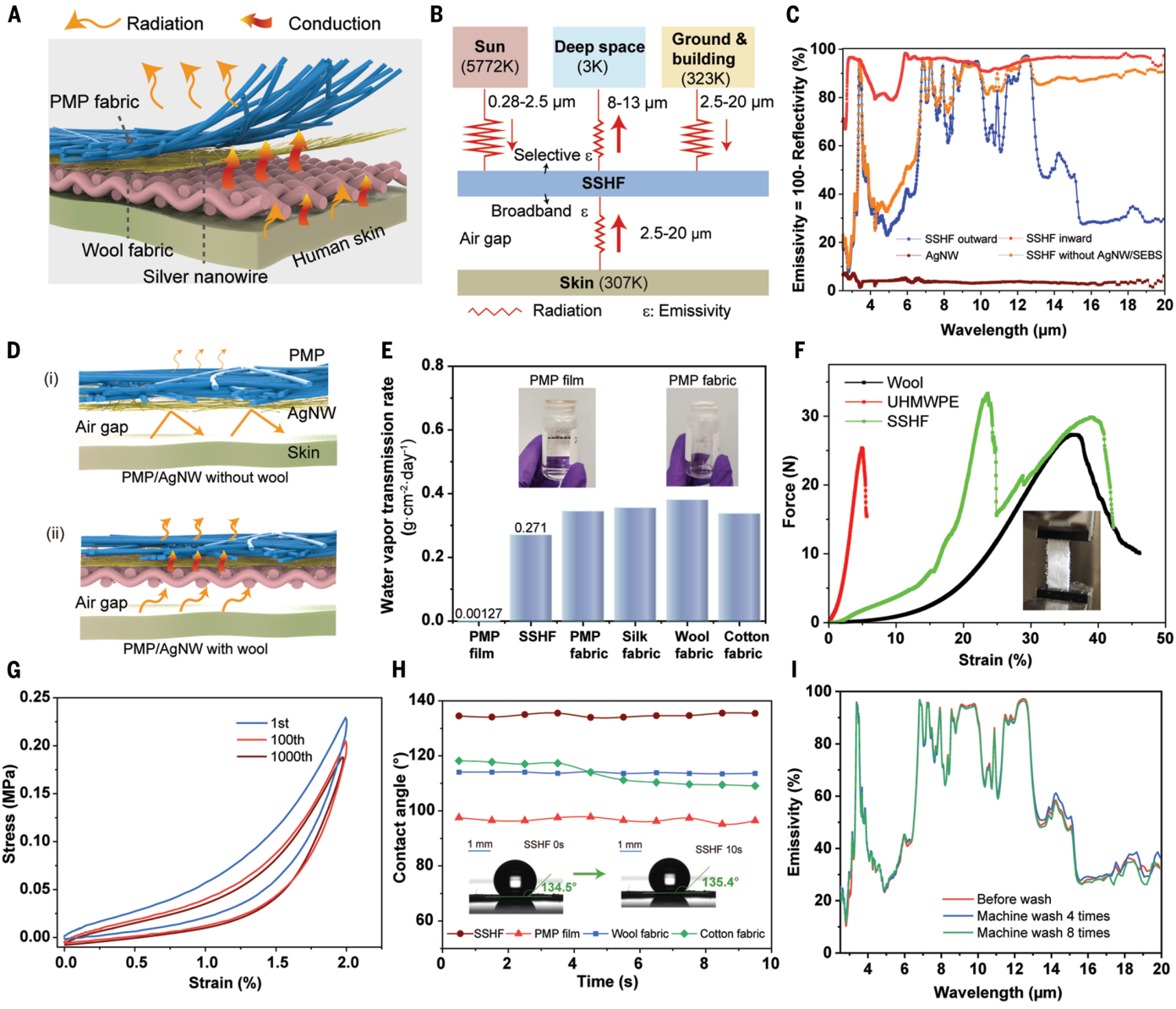

Fig. 3. Structure and wearable properties of SSHF. (**A**) Structure of the multilevel SSHF composed of PMP fabric, AgNW, and a wool fabric layer. (**B**) Radiative heat transfer network of SSHF in outdoor environments. Note that convective and conductive heat transfer are not shown for simplicity. (**C**) MIR emissivity of SSHF (measured from the top and bottom surfaces), PMP, and AgNW. SSHF shows a selective emissivity on the outward-facing side and a broadband emissivity on the inward-facing side. (**D**) Schematic showing the impact of wool fabric on the absorption of thermal radiation emitted from the human skin. (**E**) Water-vapor transmission analysis showing that the SSHF has a decent air permeability. The inset photos show the water levels for PMP film (left) and PMP fabric (right) after 30 days. (**F**) Tensile strength of SSHF, wool fabric, and UHMWPE. (**G**) SSHF shows excellent stability during 1000 stretch-and-release cycles with a strain of 2%. (**H**) Hydrophobic performance of SSHF with a contact angle of ~135°, which shows a self-cleaning capability to maintain the spectral selectivity. (**I**) MIR emissivity of SSHF before and after machine washing eight times.

network (Fig. 3B). We analyzed other textiles, such as broadband emitters (*21*, *58*–*60*), broadband transparent textiles (*61*–*64*), and semitransparent selective emitters (*65*) using similar heat transfer networks (fig. S14) [see text in (*49*)]. Among them, SSHF provides an optimal radiative heat transfer design pathway for human body radiative cooling in scenarios with hot urban infrastructures. Experimentally, we deposited the AgNW network on the backside of the PMP fabric by spray coating. To enhance the mechanical property and durability, we encapsulated AgNW within a thin layer of poly(ethylene-ran-butylene)-block-polystyrene (SEBS) (fig. S15) (*49*). The AgNW layer provides MIR reflectivity against the building and ground thermal radiation, especially within the 13- to 20-μm wavelength range, which would otherwise pass through the PMP fabric and become a heat gain (Fig. 3C). Then, we sewed a broadband-emissive wool fabric to the bottom of the AgNW/PMP fabric using ultra–high-molecular-weight polyethylene (UHMWPE) yarn. Without wool fabric, the metabolic heat emitted by the human skin would be reflected by the AgNW layer within the air gap between the human skin and the textile, blocking heat exchange from the human body to the fabric (Fig. 3D). Conversely, SSHF with a bottom wool fabric absorbs thermal radiation emitted from the skin and conducts it to the surface PMP fabric via AgNW for selective thermal emission, improving the cooling capability.

The porous structure of the SSHF provides decent breathability (Fig. 3E). PMP fabric and SSHF have high water-vapor transmission rates of 0.345 and 0.271 g $(cm^2 \cdot day)^{-1}$, respectively. Therefore, these fabrics serve as efficient conduits for the natural diffusion and convection of water vapor, facilitating cooling through perspiration. Cotton and wool fabrics demonstrate comparable water-vapor transmission rates to that of PMP fabric. By contrast, the PMP film exhibits no water-vapor permeability. After 30 days, the water in the vial covered by SSHF completely evaporated, whereas the water in the vial covered by the PMP film remained (insets of Fig. 3E). Furthermore, the SSHF exhibits a robust and durable mechanical performance under tensile testing. The strain-force curve shows two characteristic peaks during stretching (Fig. 3F), which belong to the fracture of the UHMWPE sewing yarn and wool fabric. We did not observe large breaking peaks for the PMP fabric and AgNW layer because of their isotropic characteristics. After completing 1000 stretch-and-release cycles with 2% strain, the SSHF continued to exhibit excellent mechanical performance (Fig. 3G). Also, the UV-vis-NIR reflectivity and MIR emissivity after bending and stretching 100 times show no notable difference (fig. S16), demonstrating the SSHF's long-term durability for wear. The hydrophobic property (contact angle 135°) of the top PMP fabric of the SSHF imparts a self-cleaning property, which is caused by the rough surface from the nano-micro hybrid fiber network (Fig. 3H and fig. S17). The contact angle maintains a high value of 128° after 10 min. This self-cleaning capability can preserve its spectral property over extended periods of use. The SSHF also has excellent washability. MIR emissivity is preserved after eight cycles of machine-washing tests with detergent (Fig. 3I). In addition, the SSHF shows excellent sweat resistance and on-skin comfort, with no inflammation detected after 4 days of wearing (figs. S18 and S19). Additionally, to measure the stability of the SSHF in air, we conducted accelerated durability characterization under the environmental conditions of 85°C and 90 to 100% relative humidity (RH) (*49*). The emissivity spectrum for SSHF with SEBS showed no notable change after 14 days, whereas the one without SEBS exhibited an obvious increase in the wavelength range of 13 to 20 μm, which was caused by oxidation of the AgNWs. SEBS encapsulation ensures that the SSHF has excellent oxidation durability in air (fig. S20). The SSHF also exhibits exceptional resistance to UV aging. Its multispectral property barely changed after direct exposure to a 350-W m^{-2} UV lamp for 1 week, equivalent to approximately half a year of direct sunlight exposure (fig. S21). These outstanding properties indicate that the SSHF should be durable with good wearability over time.

Outdoor thermal measurements

We demonstrated the outdoor radiative cooling performance of the SSHF by direct thermal measurements in Apache Junction, Arizona, and Chicago, Illinois. To ensure a precise and uniform measurement, we continuously monitored the textile temperature in real time using thermistors affixed to a copper plate. We used polystyrene foam for thermal insulation. To minimize sunlight absorption, we shielded the entire device with aluminum foil and silver mylar, except for the sample area (Fig. 4, A to C) [see text in (*49*)]. We measured temperatures for both vertically and horizontally oriented samples (Fig. 4C). For the horizontal test, we tilted the apparatus 15° toward the west (Fig. 4D). Near-24-hour continuous measurement demonstrated that the SSHF consistently exhibited a lower temperature than ambient temperature under clear sky conditions on 28 May 2023 at Apache Junction. During the nighttime, the SSHF yielded a subambient temperature decrease of 12.6°C on average. Even during daytime, when subjected to solar intensities of 1010 W m^{-2}, the SSHF managed to maintain a large temperature difference of 6.2°C (Fig. 4D). This value highlights the impressive cooling performance of the SSHF throughout both day and night conditions. Even in a situation with high RH, such as approximately 70% RH with total precipitable water of 22.8 mm [see text in (*49*)] on 4 May 2023 in Chicago, the daytime subambient temperature drop was still around 2.5°C (fig. S22). We then compared the temperature difference between commercialized textile materials and the SSHF when vertically placed toward S178°E. At 12:30 p.m. MST, SSHF, silk, cotton, and rubber temperatures were 40.4°, 43.8°, 44.1°, and 44.6°C, respectively (Fig. 4E). We attribute the pronounced cooling performance of SSHF to its ability to simultaneously emit heat to outer space while selectively blocking thermal radiation from the ground (>60°C) (fig. S23). We calculated the ground temperature based on the heat transfer model and the monitored meteorological data (i.e., solar intensity, RH, and ambient temperature) (fig. S24C) [see text in (*49*)]. As expected, the ground was an intense heat source for vertically facing textiles, which makes selective-spectrum engineering critical to achieving radiative cooling. To mitigate the influence of solar absorbance on the comparison of cooling performance, we prepared a reference sample with a high solar reflectivity of 90% and broadband emissivity of 92% for an outdoor daytime temperature comparison (fig. S25). We carried out both daytime and nighttime measurements with a simulated hot ground (figs. S26 and S27) from 18 to 21 December 2023 at Apache Junction. At nighttime, the SSHF was 0.2°C cooler than the broadband emitter (Fig. 4F). In addition, it showed a 4.7 W m^{-2} higher cooling power than the broadband emitter (fig. S28) [see text in (*49*)]. This directly demonstrates the radiative cooling advantage of the selective emitter in an urban scenario. During daytime, the SSHF was 2.3° and 8.9°C cooler than the broadband emitter and commercialized silk fabric, respectively (fig. S26C). This cooling performance results from both the high solar reflectivity and MIR selective emissivity of the SSHF.

To further demonstrate the cooling effect of the SSHF under realistic wearing conditions, we used a heater to simulate the metabolic heat of the human body by applying a consistent power of 115 W m^{-2} (*21*, *66*). The temperatures for the SSHF, silk, cotton, and rubber were 49.4°, 51.6°, 52.5°, and 52.2°C respectively at 4:30 p.m. MST (Fig. 4G). These results again show the superior cooling performance of the SSHF compared with that of commercial fabrics. In addition, we conducted on-skin measurements by having a volunteer wear the SSHF and cotton fabric on either arm on 13 April 2024 at Apache Junction. Skin temperature was measured using thermistors attached to the skin underneath the fabrics. The SSHF was approximately 1.8°C cooler than the cotton fabric, further verifying the on-skin

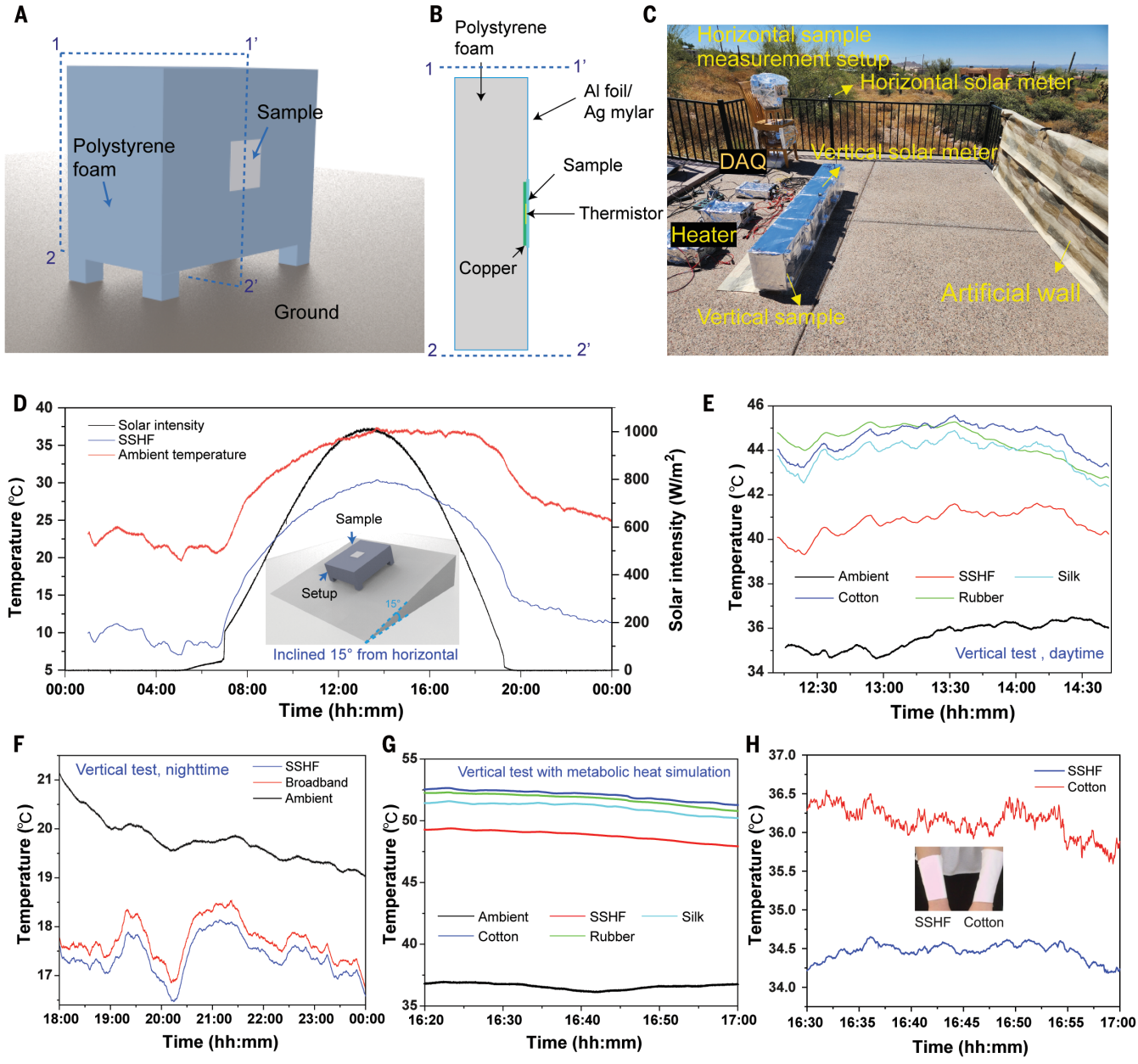

Fig. 4. Outdoor thermal measurements of SSHF and various common textile samples. (**A** and **B**) Overall (A) and cross-sectional (B) schematics of the vertical measurement apparatus. (**C**) Photo of the experimental setup used for the outdoor thermal measurements at Apache Junction, Arizona (33.44° N, 111.48°W, elevation of 635 m). DAQ, data acquisition. (**D**) Near-all-day continuous measurement of the subambient radiative cooling performance on 28 May 2023. The inset is a schematic showing the measurement setup tilted 15° from the horizon. (**E**) Temperature of different vertically oriented samples measured on 27 May 2023. (**F**) Temperature comparison of a vertically placed SSHF and broadband emitter at nighttime on 18 December 2023. (**G**) Temperature of different vertically oriented samples with metabolic heat simulation on 28 May 2023. (**H**) Temperature tracking of the skin of a volunteer wearing SSHF and commercialized cotton fabric on either arm, measured on 13 April 2024. The inset photo shows the volunteer wearing the fabrics.

cooling effect of the SSHF in urban scenarios (Fig. 4H).

Radiative cooling textiles in urban areas are essential because of the increasing heat island effect. To extrapolate the cooling performance of the SSHF in urban scenarios, we built a three-dimensional (3D) theoretical model and calculated the impact of the building view factors on the human body under different scenarios. We defined the view angle β as the angle between the horizon and the line connecting the textile and the top corner of the building facade and φ as the angle between the bottom center and bottom side of the building (assuming the building is symmetric) (Fig. 5A). We regarded the view angle β to be consistent along the vertical direction, considering that the height of the human body is small compared with that of the buildings in urban areas. Assuming the human is at the center of the building facade, the 3D view factors of the textile to the sky and terrestrial features [including ground and buildings; see text in (*49*)] are shown in Fig. 5B. In an open scenario (β = 0°, and φ = 0°), the view factor to the sky and terrestrial features are both 0.5. As β and φ increase, the view factor to the infrastructure

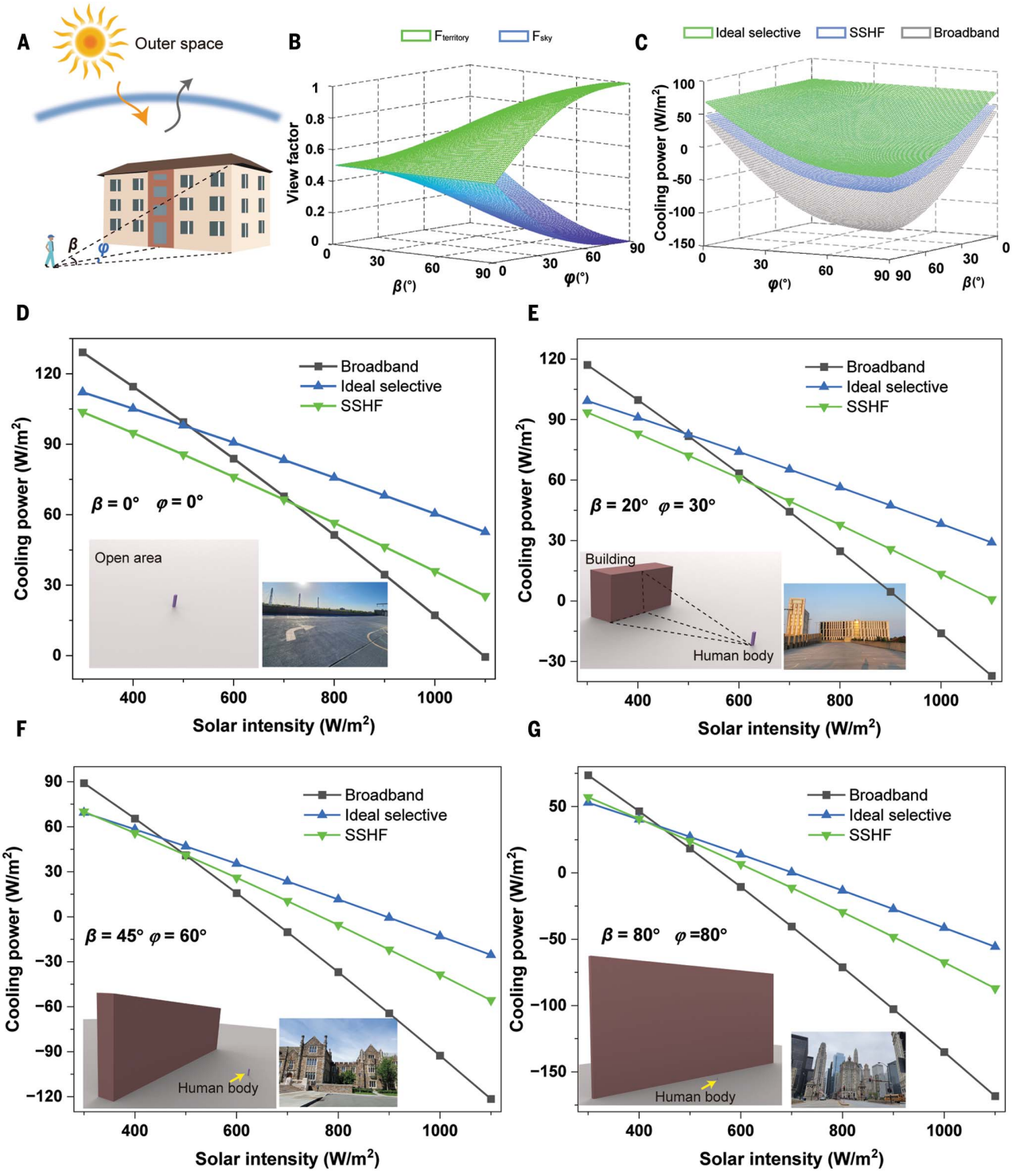

Fig. 5. Cooling power comparison of SSHF, a broadband emitter, and an ideal selective emitter in different urban scenarios. (**A**) Schematic of the view angles of the building, β and φ, in the urban scenario. (**B**) Calculation results demonstrating that the view factor from a vertically oriented textile to the territorial features ($F_{territory}$) increases from 0.5 to 1, whereas that to the sky (F_{sky}) decreases from 0.5 to 0 when the angles of building views β and φ are changed from 0° to 90°. (**C**) Calculation results for cooling power for SSHF, a broadband emitter, and an ideal selective emitter as a function of β and φ. (**D** to **G**) Calculated cooling power at different urban scenarios with β = 0 and φ = 0° (D), β = 20 and φ = 30° (E), β = 45 and φ = 60° (F), and β = 80 and φ = 80° (G). The inset images show a diagram (left) and corresponding real-world example (right) of typical urban scenarios.

objects becomes larger and reaches unity when β = 90° and φ = 90°. We theoretically compared the cooling power of the SSHF with that of a broadband fabric under a solar intensity of 850 W m^{-2} in an open scenario (Fig. 5C). The SSHF consistently exhibited a higher cooling power than the broadband textile. With β and φ both increasing from 0° to 90°, the difference in cooling power between the

SSHF and broadband textile further increased from 8.5 to 59.6 W m^{-2}. To further predict the cooling performance in complicated urban scenarios with various building densities, we built a 3D model using COMSOL Multiphysics (fig. S29) [see text in (*49*)]. We took into consideration the thermal and photonic parameters for both building and ground, such as thermal resistance, heat capacity, emissivity, and solar reflectivity. The SSHF supplies a higher cooling power than the broadband fabric at a solar intensity of 400 W m^{-2} at different building densities, with two to six buildings surrounding the human body (fig. S30). The performance gap becomes larger when the buildings get higher (fig. S30D).

In addition, we experimentally tested the cooling effect with outdoor measurements by using wallpaper (with a height of 0.68 m) to simulate an urban scenario (Fig. 4C). We set the distance between the textile and wall at 1.86 m. The temperatures for the SSHF, silk, cotton, and rubber were 40.9°, 42.5°, 44.1°, and 44.6°C, respectively, at 3:30 p.m. MST on 27 May 2023 (fig. S31). This further demonstrates that SSHF is a promising textile for outdoor personal thermoregulation in urban areas.

Our overall strategy is flexible because different layers can be changed to improve metrics, such as ATW emissivity, which may promote cooling performance. For example, in an open scenario such as plain ground in Levant, Kansas, when the solar intensity is 1000 W m^{-2}, the SSHF has the potential to yield an additional 18.8 W m^{-2} of cooling power compared with a broadband emitter (Fig. 5D). Under the same illumination conditions with $\beta = 20°$ and $\varphi = 30°$ (e.g., on a street near a three-floor building), $\beta = 45°$ and $\varphi = 60°$ (e.g., on a street near an eight-floor building), and $\beta = 80°$ and $\varphi = 80°$ (e.g., near a high-rise building in a downtown city), the SSHF outperforms the broadband emitter with additional cooling powers of 29.4, 54.2, and 67.4 W m^{-2}, respectively, which correspond to 54.3, 68.1, and 72.2% of that which can be realized by an ideal selective emitter (Fig. 5, E to G). In other words, the use of more-advanced spectrum engineering to approach the ideal selectivity would further boost the cooling performance, especially in scenarios with low β and φ (such as plain ground or suburban areas).

Conclusions

We developed a spectrum-engineered hierarchical textile that has selective emissivity greatly dominant in the ATW on the outward-facing side and broadband emissivity on the inward-facing side. The high emissivity in the ATW region allows the SSHF surface to emit heat to outer space, and high reflectivity (low absorptivity) in the non-ATW region minimizes the heat gain from the hot surroundings, such as the ground and buildings. Meanwhile, the high inward-facing broadband emissivity facilitates radiative heat exchange with the human body, in parallel to air-gap conduction and convection. The SSHF features a high solar reflectivity of 0.97 due to the strong Mie scattering from the nano-micro hybrid fibrous structure. The rational optical design and fiber nanofabrication enable substantial cooling effects: The SSHF is 2.3°C cooler than the broadband emitter when placed vertically and 6.2°C cooler than the ambient temperature when placed horizontally. Meanwhile, the SSHF exhibits excellent wearability, including breathability, washability, durability, robust mechanical properties, and an anti-UV aging property. Supported by a comprehensive heat transfer analysis between individuals and their environment, our selective-spectrum design for vertical-facing textiles introduces an innovative and effective solution for passive personal cooling to counter the urban heat island effect, a solution that not only holds the potential to curtail air-conditioning energy consumption but also serves as a preventive measure against heat-related health issues.

REFERENCES AND NOTES

1. D. Oudin Åström, B. Forsberg, K. L. Ebi, J. Rocklöv, *Nat. Clim. Chang.* **3**, 1050–1054 (2013).
2. E. Pennisi, *Science* **370**, 778–781 (2020).
3. R. P. Woychik *et al*., *Lancet* **400**, 1831–1833 (2022).
4. R. Wu, T. Chen, P. Hsu, *EcoMat* **5**, e12396 (2023).
5. G. Manoli *et al*., *Nature* **573**, 55–60 (2019).
6. R. D. Bornstein, *J. Appl. Meteorol. Climatol.* **7**, 575–582 (1968).
7. L. Zhao, X. Lee, R. B. Smith, K. Oleson, *Nature* **511**, 216–219 (2014).
8. J. J. Lembrechts, I. Nijs, *Science* **368**, 711–712 (2020).
9. M. Santamouris *et al*., *Energy Build.* **166**, 154–164 (2018).
10. L. Zhao *et al*., *Environ. Res. Lett.* **13**, 034003 (2018).
11. E. E. Stache, B. B. Schilperoort, M. M. Ottelé, H. H. Jonkers, *Build. Environ.* **213**, 108489 (2022).
12. C. Sarrat, A. Lemonsu, V. Masson, D. Guédalia, *Atmos. Environ.* **40**, 1743–1758 (2006).
13. S. C. Sherwood, *Science* **370**, 782–783 (2020).
14. E.-S. Im, J. S. Pal, E. A. B. Eltahir, *Sci. Adv.* **3**, e1603322 (2017).
15. A. Cosgrove, M. Berkelhammer, *NPJ Clim. Atmos. Sci.* **1**, 46 (2018).
16. S. E. Berger *et al*., *Sci. Rep.* **13**, 10061 (2023).
17. D. Li *et al*., *Sci. Adv.* **5**, eaau4299 (2019).
18. C. M. Profiroiu, D. A. Bodislav, S. Burlacu, C. V. Rădulescu, *Eur. J. Sustain. Dev.* **9**, 51–57 (2020).
19. J. Yang, L. Hu, C. Wang, *Sci. Adv.* **5**, eaay3452 (2019).
20. J. Liang *et al*., *Natl. Sci. Rev.* **10**, nwac208 (2022).
21. S. Zeng *et al*., *Science* **373**, 692–696 (2021).
22. J. Mandal *et al*., *Science* **362**, 315–319 (2018).
23. M. Chen *et al*., *Nano Lett.* **21**, 1412–1418 (2021).
24. J. Yun *et al*., *ACS Photonics* **10**, 2608–2617 (2023).
25. Z. Li, Q. Chen, Y. Song, B. Zhu, J. Zhu, *Adv. Mater. Technol.* **5**, 1901007 (2020).
26. X. Zhao *et al*., *Cell Rep. Phys. Sci.* **3**, 100853 (2022).
27. K. Tang *et al*., *Science* **374**, 1504–1509 (2021).
28. X. Li *et al*., *Cell Rep. Phys. Sci.* **1**, 100221 (2020).
29. P.-C. Hsu, X. Li, *Science* **370**, 784–785 (2020).
30. A. Leroy *et al*., *Sci. Adv.* **5**, eaat9480 (2019).
31. K. Zhou *et al*., *Nano Lett.* **21**, 1493–1499 (2021).
32. Y. Zhai *et al*., *Science* **355**, 1062–1066 (2017).
33. S. Wang *et al*., *Science* **374**, 1501–1504 (2021).
34. H. Liu, J. Yu, S. Zhang, B. Ding, *Nano Lett.* **22**, 9485–9492 (2022).
35. Q. Zhang *et al*., *Small Methods* **6**, e2101379 (2022).
36. L. Zhou *et al*., *Nat. Sustain.* **2**, 718–724 (2019).
37. K. Li *et al*., *Small* **19**, e2206149 (2023).
38. T. Li *et al*., *Science* **364**, 760–763 (2019).
39. X. Zhang *et al*., *ACS Nano* **16**, 2188–2197 (2022).
40. W. Xie *et al*., *Adv. Funct. Mater.* **33**, 2305734 (2023).
41. P. Liu *et al*., *ACS Appl. Electron. Mater.* **5**, 5755–5776 (2023).
42. M. Li, Z. Yan, D. Fan, *ACS Appl. Mater. Interfaces* **15**, 17848–17857 (2023).
43. S. Wang *et al*., *Small* **20**, e2305706 (2023).
44. C. D. Fryar, M. D. Carroll, Q. Gu, J. Afful, C. L. Ogden, *Anthropometric Reference Data for Children and Adults: United States, 2015–2018*, Vital and Health Statistics, Series 3 (National Center for Health Statistics, 2021).
45. E. Gazzuolo, M. DeLong, S. Lohr, K. Labat, E. Bye, *Appl. Ergon.* **23**, 161–171 (1992).
46. A. C. Chui, A. Gittelson, E. Sebastian, N. Stamler, S. R. Gaffin, *Urban Clim.* **24**, 51–62 (2018).
47. J. Mandal, S. Mandal, J. Brewer, A. Ramachandran, A. P. Raman, arXiv:2006.11931 [physics.app-ph] (2020).
48. Z. Ma, D. Zhao, F. Wang, R. Yang, *Energy Build.* **258**, 111842 (2022).
49. Materials and methods are available as supplementary materials.
50. X. Yin, R. Yang, G. Tan, S. Fan, *Science* **370**, 786–791 (2020).
51. D. Li *et al*., *Nat. Nanotechnol.* **16**, 153–158 (2021).
52. S. Fan, W. Li, *Nat. Photonics* **16**, 182–190 (2022).
53. A. P. Raman, M. A. Anoma, L. Zhu, E. Rephaeli, S. Fan, *Nature* **515**, 540–544 (2014).
54. A. Aili *et al*., *Mater. Today Phys.* **10**, 100127 (2019).
55. Y. Tian *et al*., *Sci. Rep.* **9**, 19317 (2019).
56. J. Feng *et al*., *Sol. Energy Mater. Sol. Cells* **234**, 111419 (2022).
57. P.-C. Hsu *et al*., *Sci. Adv.* **3**, e1700895 (2017).
58. D. Miao, N. Cheng, X. Wang, J. Yu, B. Ding, *Nano Lett.* **22**, 680–687 (2022).
59. X. Zhang *et al*., *ACS Photonics* **10**, 1624–1632 (2023).
60. P. Yao *et al*., *Adv. Mater.* **34**, e2208236 (2022).
61. P. C. Hsu *et al*., *Science* **353**, 1019–1023 (2016).
62. Y. Fang, X. Zhao, G. Chen, T. Tat, J. Chen, *Joule* **5**, 752–754 (2021).
63. L. Cai *et al*., *Adv. Mater.* **30**, e1802152 (2018).
64. Y. Peng *et al*., *Nat. Sustain.* **1**, 105–112 (2018).
65. X. Wu *et al*., *Nat. Sustain.* **6**, 1446–1454 (2023).
66. B. Zhu *et al*., *Nat. Nanotechnol.* **16**, 1342–1348 (2021).

ACKNOWLEDGMENTS

This work made use of the shared facilities at the University of Chicago Materials Research Science and Engineering Center, which are supported by the National Science Foundation under award no. DMR-2011854. Parts of this work were carried out at the Soft Matter Characterization Facility of the University of Chicago. We acknowledge J. Gibson from the University of Illinois Urbana-Champaign for nano-CT image scanning; A. Berk from Spectral Sciences, Inc., for his help in calculating atmospheric spectral transmittance; and Shinkong textile and City Victor Corp for providing cotton and nylon fabrics. R.W. acknowledges G. and N. Jonson for providing the locations for outdoor experiments in Arizona. **Funding:** The project is partially sponsored by the startup fund of the Pritzker School of Molecular Engineering, University of Chicago. P.-C.H. and P.-J.H. received funding from the National Science Foundation (Electrical, Communications and Cyber Systems award no. 2145933). Z.Z. and D.V.T. received support from the US Department of Defense, Air Force Office of Scientific Research, under grant FA9550-22-1-0283. **Author contributions:** P.-C.H. and R.W. conceived the idea. R.W. performed sample preparation, characterizations, cooling power calculations, and corresponding data analyses. C.S. performed emissivity and outdoor cooling power simulations. T.-H.C. performed spectroscopic ellipsometry and refractive indices extractions. Q.L. performed scattering efficiency calculations. Z.Z. and D.V.T. helped with setting up the integrating sphere for the UV-vis-NIR measurements; G.Y. and Y.H. helped with SEM characterization; J.L., P.-J.H., Q.L., and G.Y. helped with sample preparation; and C.S. and E.L. helped with the

outdoor experiments. R.W., C.S., and P.-C.H. wrote the manuscript with input from all co-authors. **Competing interests:** P.-C.H. and R.W. have filed a patent application related to this work. **Data and materials availability:** All data are available in the main text or the supplementary materials.

SUPPLEMENTARY MATERIALS

science.org/doi/10.1126/science.adl0653
Materials and Methods
Supplementary Text
Figs. S1 to S32
Tables S1 to S4
References (*67*–*84*)

Submitted 26 September 2023; accepted 7 May 2024
10.1126/science.adl0653